BNL-67213

Detector Challenges for $\mu^+\mu^-$ Colliders in the 10–100 TeV Range

presented by Pavel Rehak* for D. Cline**, E. Gatti†, C. Heusch⊕, S. Kahn*, B. King*, T. Kirk*, P. Norton‡, V. Radeka*, N. Samios*, V. Tcherniatine* and W. Willis◇

*Brookhaven National Lab., Upton NY 1973-5000[1]
**Univ. of California, Dept. of Physics, 405 Hilgard Ave, LA, CA 92717
†Politecnico di Milano, P.za L.da Vinci 32, 20133 Milano,Italy
⊕Stanford Linear Accelerator Center, P.O. Box 4349, Stanford, CA 94309
‡Rutherford Appleton Lab., Chilton, Didcot, Oxon. OX11 0QX, England
◇Nevis Labs, Columbia Univ., P.O.Box 137, Irvington-on Hudson, NY 10533

Abstract. The challenges to design, construct and operate a detector system in an interaction region at a high energy $\mu^+\mu^-$ collider are briefly summarized. A new solution, based on an extensive use of liquefied rare gases, is proposed for the vertex detector and for the inner tracker. The proposed solution takes a full advantage of the small size of the collision region. The region has radial dimensions below the μm range, while its extent in the beam direction is of the order of $1mm$ depending on the energy of the machine and on the details of the design. In the energy range considered in this workshop, the momenta of charged particles are high enough to be bent only slightly in the solenoidal magnetic field. The tracks are basically straight lines emerging from a known common point. The proposed solution is based on a projective geometry matched to the desired tracks. The aim of the design is to achieve a background blind radiation hard detector.

The second novel feature of the design is the calorimetric instrumentation of two large 20^o tungsten cones used to shield the detector from the machine induced background. Here again the full advantage of the known directionality of particles initiating the shower process is incorporated into the design.

INTRODUCTION

The main challenge for the detector system around an intersection region of a $\mu^+\mu^-$ collider is to eliminate background particles reaching the detector practically at the same time as the particles of interest. There are three sources of background particles:

1. muon halo

[1] Supported by Department of Energy contract DE–AC02–98CH10886

TABLE 1. Radial Fluences at $2 \times 2TeV$. Numbers of particles crossing a radial surface of $1cm^2$ for two bunches of $10^{12}\mu's$ each

Radius (cm)	photons	neutrons	protons	pions	electrons	muons
5	2700	120	0.05	1.8	2.3	1.7
10	750	110	0.20	0.8		0.7
15	350	100	0.13	0.8		0.4
20	210	100	0.13	0.6		0.1
50	70	120	0.08	0.1		0.02
100	31	50	0.04	0.006		.008
calor.						.003
muon s.						.0003
cut–off	25	40	10	10		
threshold	keV	keV	MeV	MeV		

2. decays of the muon beams producing high energy electrons

3. beam–beam interactions

Detailed studies of individual background sources and the design of the shielding of the intersection region were carried for center-of-mass (COM) energies of 0.1, 0.5 and 4 TeV [1,2]. The shielding for the highest COM energy of 4 TeV was designed already in 1996. [1] Since then there has been a better understanding of the shielding geometry and an improved configuration was designed for lower energy $\mu^+\mu^-$ colliders. The decrease in fluences of background particles is about a factor of two. It was also found out that the background fluences decrease with the increase of the beam energy for the same number of muons in the bunch. In this paper, however, we will take the background fluences from studies [1], listed in Table 1, to be more conservative.

The most direct impact of the shielding on the design of the detector are two conical tungsten shields with angles up to 20^o, called noses, coming very close to the intersection region. During the discussions within the working group it become apparent that it is advantageous to instrument both cones (noses). The most important new technology proposed in this workshop is the "Background blind, radiation hard" vertex detector and tracker. This technology takes full advantage of i) the small size of the interaction point of the $\mu^+\mu^-$ collider and ii) the time structure of the signal and background. The view of an elementary cell is shown in Figure 1. The detection medium is liquid argon or neon. This medium is radiation hard and allows to fill almost any geometry. The electric field applied to the cell is such that signal electrons move across the short cell dimension ($2mm$). The collection time is about $1\mu s$, that is, short enough relative to the bunch crossing time. The shown cell points to the intersection region and the aspect ratio of the cell depth to the transverse dimensions leads to a large background suppression already from the rough ionization measurement.

Most of the paper will be dedicated to the analysis of the performance of the detector built from close packages of these cells. With prior knowledge of the direc-

tion of electromagnetic showers were electrons and γ's originated at the intersection point, the segmentation of the calorimeter was also optimized to take full advantage of the shower directionality. Driven by physics one can even think about an almost fully absorbing liquid xenon electromagnetic calorimeter.

This contribution starts with an overall description of the detector. Most considerations are for the $10TeV$ option. The main section presents a detail analysis of the new vertex detector and the new tracker. All possible limitations of the vertex detector are analyzed. The section about calorimetry emphasizes a possible construction with a high degree of directional selectivity. The Appendix shows a very good position resolution attainable with the cells of the proposed vertexer and tracker.

DETECTOR SYSTEMS

A cross section of the "Strawman Detector" (from [1]) is shown in Figure 2. The dimensions shown on the Figure 2 are only rough indications, as they would be different for different beam energies in order to fit between the two last quadrupoles. The detector has a solenoidal magnetic field and consists of following 6 components:

1. Vertex Detector
2. Inner Tracker Detector of charged particles
3. Instrumented Tungsten shield as a Calorimeter
4. Electromagnetic Calorimeter
5. Hadron Calorimeter

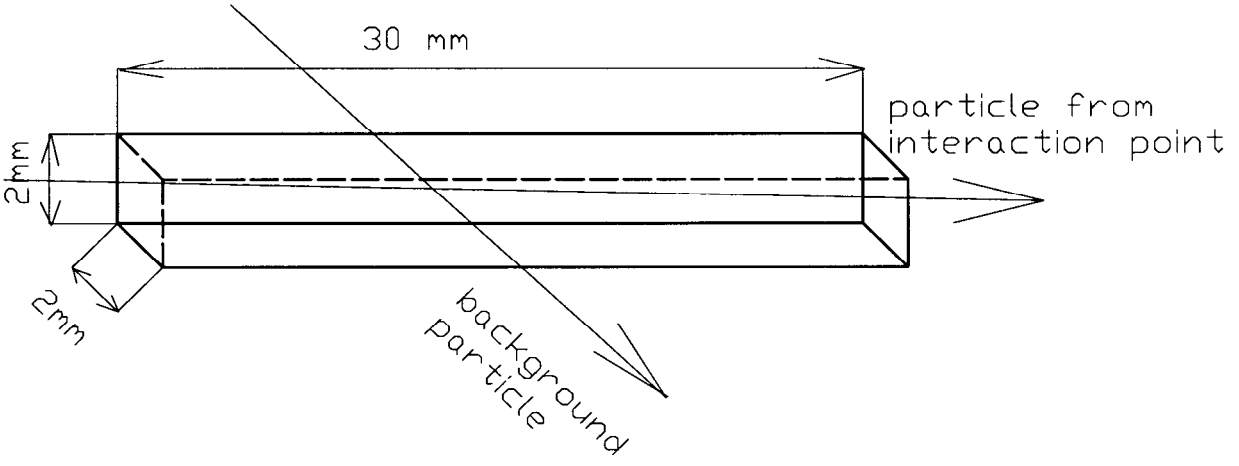

FIGURE 1. Basic cell of the vertex detector and tracker. Particles from the interaction point traverse the cell along the long direction producing a large signal charge. Ionization within the cell due to background particles is much smaller.

6. Muon Spectrometer

The first attempt to specify criteria for the detector in the high muon energy range is summarized in Table 2. A solenoid is the natural choice for interaction with almost isotropic distribution of track of interest. The strength of the field may be increased for a higher energy machine and the actual field depends on the state of the magnet technology at the time of the construction. The coil placement behind the hadron calorimeter is not fixed. The need of a higher magnetic field in the inner tracker may move the coil right behind the electromagnetic calorimeter.

A new vertex detector and a new inner tracker are being proposed here. These systems take full advantage of the small extent of the intersection region and the time structure of the bunch crossings.

The instrumentation of the nose of the tungsten shield is the other novel feature of this report. It is felt that the physics potential of the $\mu^+\mu^-$ detector can be greatly enhanced by it. Most importantly, even a coarse measurement of electromagnetic

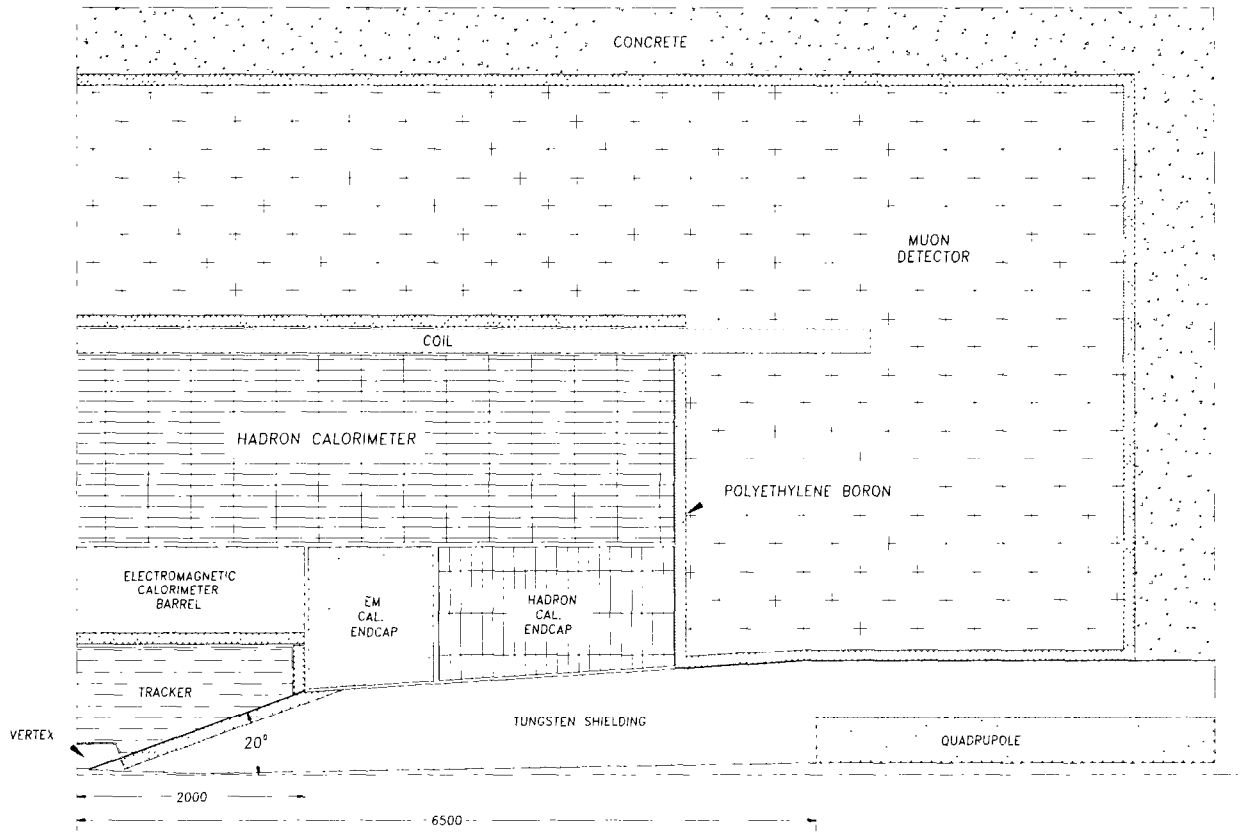

FIGURE 2. Strawman detector

TABLE 2. Detector Performance Requirements. (10 TeV)

Detector Component	Minimum Resolution/Characteristics
Magnetic field	Solenoid; $B > 3T$
Vertex Detector	b-tagging; $\sigma \lesssim 10\mu m$; small cells
Inner Tracker	$\Delta p/p^2 \lesssim 2 \cdot 10^{-4}(GeV)^{-1}$ at large p High granularity background blind
Nose calorimeter	$\Delta E/E \sim 35\%/\sqrt{E} \oplus 4\%$ for EM showers $\Delta E/E \sim 70\%/\sqrt{E} \oplus 8\%$ for hadron showers
EM Calorimeter	$\Delta E/E \sim 10\%/\sqrt{E} \oplus 0.7\%$ (baseline) $\Delta E/E \sim 5\%/\sqrt{E} \oplus 0.4\%$ maybe required projective geometry. Depth $\sim 25X_0$
Hadron Calorimeter	$\Delta E/E \sim 60\%/\sqrt{E} \oplus 3\%$ Granularity: projection cells and transverse Total depth (EM + HAD)$\gtrsim 7\lambda$
Muon Spectrometer	$\Delta p/p \lesssim 15\%$ at 1TeV Combining with the Inner Tracker

and hadron energies will improve considerably the detection of missing transverse energy. The importance of identifying and of measuring the missing energy is reported by the theory working group of this workshop.

There are two versions of the Electromagnetic calorimeter considered. Both versions identify electrons, photons and the core of jets. The projection geometry and the granularity are crucial to reduce the background. The first, baseline version is a sampling calorimeter. The second, that is, the high performance version of the calorimeter may be required by physics. A possible realization of such a high resolution would be an almost fully absorbing liquid xenon Electromagnetic calorimeter.

The hadron calorimeter measures jets with enough precision to separate W's from Z^0s and provide an indication of the missing transverse energy. It is a very large and expensive detector and whose not many details are given in this report. It is located in a region well shielded from the radial flux of background particles originating in the nose of the tungsten shield. Due to its large transverse dimensions it intercepts high flux of longitudinal muons. The segmentation of the hadron calorimeter may be different from the segmentation of the electromagnetic one due to different background profiles and also due to different shapes of hadron and electromagnetic showers.

The muon spectrometer, located outside the hadron calorimeter, and an additional shielding, identifies and measures muons. The momentum measurement of muons is the combination of the momentum measurement in the inner tracker and in the muon system itself. Due to the background flux of the muons moving mainly parallel to the beam directions a high degree of redundancy is required.

VERTEX DETECTOR

Main Design

The vertex detector is based on liquid noble gases rather than on silicon as the detection medium for the following reasons:

1. radiation hardness
2. ability to deliver position resolution down to a few μm range
3. formation of long detection cells pointing to the interaction region leading to superior background rejection.

The vertex detector is the nearest detector to the beams and is most exposed to radial backgrounds. At the same time it has the most demanding performance specifications. The task of the vertex detector is to identify secondary vertices created mainly B and τ decays and measure the points on the trajectories of charge tracks close to the collision point.

The proposed vertex detector is shown in Figure 3. It is based on long and narrow individual cells, closely packed, pointing in both z and ϕ coordinates directly to the intersection point. The high aspect ratio between the depth and the transverse dimension of the cell is possible thanks to the small extent of the intersection region. The size of the intersection region is only a few μm in the transverse dimensions and about a mm along the direction of the beams. The tracks of interest, having fairly high momentum have a very small curvature in the scale of the Figure 3. Individual cells have a typical ratio of depth to transverse dimension of about 15.

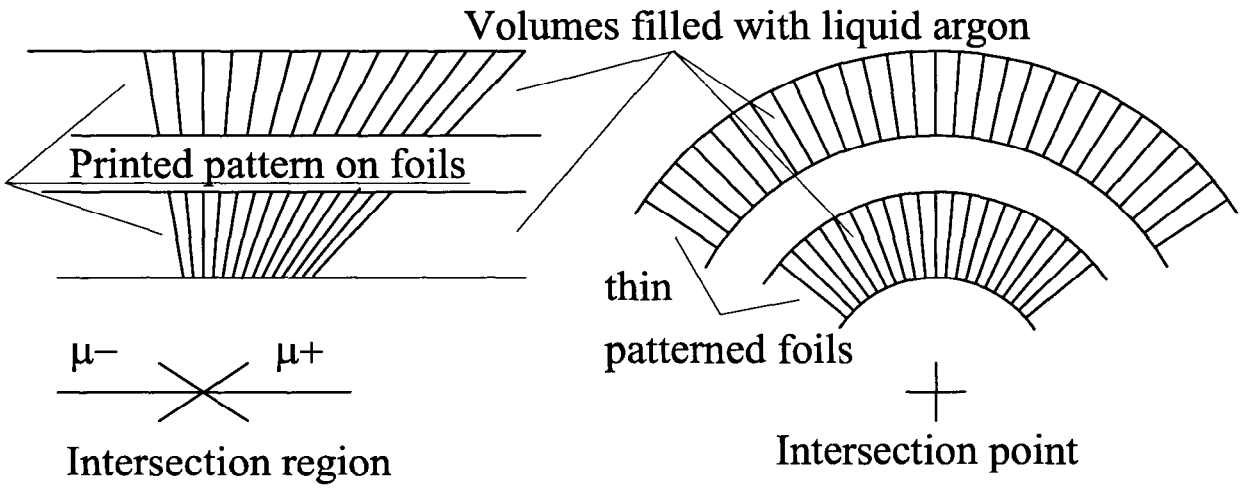

FIGURE 3. Cross sections through the vertex detector. The first layer starts at a distance of about 4cm. A typical transverse dimension of a cell is 2mm, the length of the cell 3cm. Electric field is applied perpendicular to the radial direction leading to a short collection path for signal electrons.

TABLE 3. Effective thresholds for different detection media

Detection medium and detector	Typical energy threshold
Gas proportional counters	$\sim 100eV$
Silicon planar detectors	$\sim 10keV$
Long liquid argon cells	$\sim 1MeV$

The energy deposited within a cell by a charge particle originating at or close to the interaction region is thus substantially larger than background tracks leading to the background rejection (see below) already at the single hit level before the additional constraint of combining hits into segments of a track.

The proposed approach can be seen as an extension of the concept of pixel micro-telescopes [2,3]. Here the detection medium, being liquid argon or liquid neon, allows perfectly projective shape pointing into the interaction region and the extension of the detection depth by two orders of magnitude from $300\mu m$ for a typical silicon layer to a few cm. A minimum ionizing particle deposits about $6Mev$ in $3cm$ of liquid argon. The effective thresholds for charged particles in gas, silicon and liquid argon are given in Table 3. We can see that the effective threshold in the proposed long liquid argon cell is 2 orders of magnitude higher than in a typical silicon detector and 4 orders of magnitude higher than in a gas detector. In the large background environment of the $\mu^+\mu^-$ collider this feature contributes to the early background rejection.

The electric field is applied in a direction perpendicular to the direction of the particle produced in the intersection region. The charge carriers, that is, electrons and positive ions produced by the ionization, move a relatively short distance ($\sim 1mm$) before being collected by electrodes. The maximum collection time for electrons is less than $1\mu s$. This time is much shorter than the time before the next muon bunch crossings. This time is used to process the signal waveforms due to the moving electrons. Detailed analysis in the Appendix shows that the precision of the determination of the particle crossing is about $10\mu m$ in both directions perpendicular to the direction of the charged particle.

It is stressed that this precision is attainable with liquid noble gases which are well suited as high resolution position detectors. The density of the ionization is three orders of magnitude higher in the liquid phase than in gases at atmospheric pressure and comparable to semiconductors. The liquids provide enough signal charge without the need for an avalanche amplification. More importantly, the range of delta rays is much reduced in liquids. The ionization is confined within a μm diameter column, roughly the same as in semiconductor detectors. We believe that the resolution of $10\mu m$ obtainable from the signal processing is not degraded by ionization processes in liquid noble gases.

The number of read out channels of the three layers (cylinders) is several times 10^5 with less than 10^5 channels in the closest layer to the intersection. This is a modest number of channels and connections. One can replace the electronics of the closest detection layer in case of radiation damage. The layers further away from

the interaction point receive less radiation not only because of the geometry but also due to the absorption of photons in the previous layers.

Background rejection

The first idea about the background rejection of the cell can be obtained from a simple calculation from Figure 1. It is assumed that the angular distribution of background particles is uniform in a hemisphere away from the intersection point. A background particle, crossing the entrance surface of the cell will be detected if it crosses, let us say, one half of the length of the cell. The probability of being accepted is thus $p_{acc} \approx (2mm)^2/(2\pi \cdot (15mm)^2) \approx 1\%$. The rejection can be tuned by changes of the cell geometry.

The simulated fluences of various background particles are reported in Table 1. The first layer of the vertex detector at about $5cm$ from the interaction point receives the highest density of background particles. The total density of charged background particles, that is, protons, pions, electrons and muons is about $6/cm^2$. The largest cell has the entrance surface of $2mm \times 2mm = .04cm^2$. It means that the probability for a charged background particle to enter a cell is about 0.2. The probability to produce the signal above the threshold and result in a hit in the largest cell is only 0.2%.

The flux of neutron does not represent a problem for the proposed vertex detector and tracker. There is very little energy transfered to liquid argon, or liquid neon in the interaction with a neutron. Moreover, due to the saturation effects in these liquids, the dense ionization of a slowly moving atom is not visible.

The most important background is the flux of photons. The energy spectrum of photons in the vertex region is shown in Figure 4. A Monte Carlo program was developed to study the sensitivity of the proposed vertex detector to this photon flux . The background photons were incident on the layer of the vertex detector where they interacted, mostly by Compton scattering. Trajectories of the resulting electrons were followed in the magnetic field within the cells.

The histogram of length of electron trajectories for three different cell dimension is shown in Figure 5. The resulting integral spectrum of energy deposited in a cell, normalized to 1 is shown in Figure 6 for the same geometries of the detector cells. The energy deposited by a minimum ionizing particle originating from the interaction point in 3 cm of liquid argon is about $6.6MeV$. One assumes that the threshold for individual cells is about $4MeV$. The acceptance of the photonic background in a case of $0.5mm \times 2mm$ cell is only 0.3%.

The probability of a photon conversion in the energy range of a few MeV in 1cm of liquid argon is $6.2 \cdot 10^{-2}cm^{-1}$ or about 20% in 3cm of the cell's length. Let us concentrate on the first measuring layer (cylinder) of the vertex detector about $5cm$ from the interaction region. Within one cell with an entrance area of $0.5mm \times 2mm$ there are $2700cm^{-2} \times 0.01cm^2 \times 0.2 = 5.4$ photon conversions per bunch crossing. Taking the above energy acceptance (suppression) factor of 0.3%, the mean cell

occupancy of the closest layer is about 1.6%. The occupancy decreases rapidly with the distance from the beams. Already the cells of the second layer (cylinder) can have the entrance surface $1mm \times 2mm$ with the same mean occupancy. The dimensions of the entrance areas of the subsequent layers (cylinders) is determined by requirements of the position resolution rather than background occupancy.

The mean cell occupancy can be decreased by replacing liquid argon with liquid neon as the detection medium. The photon conversion probability in this energy range is about a factor of two lower in neon than in argon. The change to neon

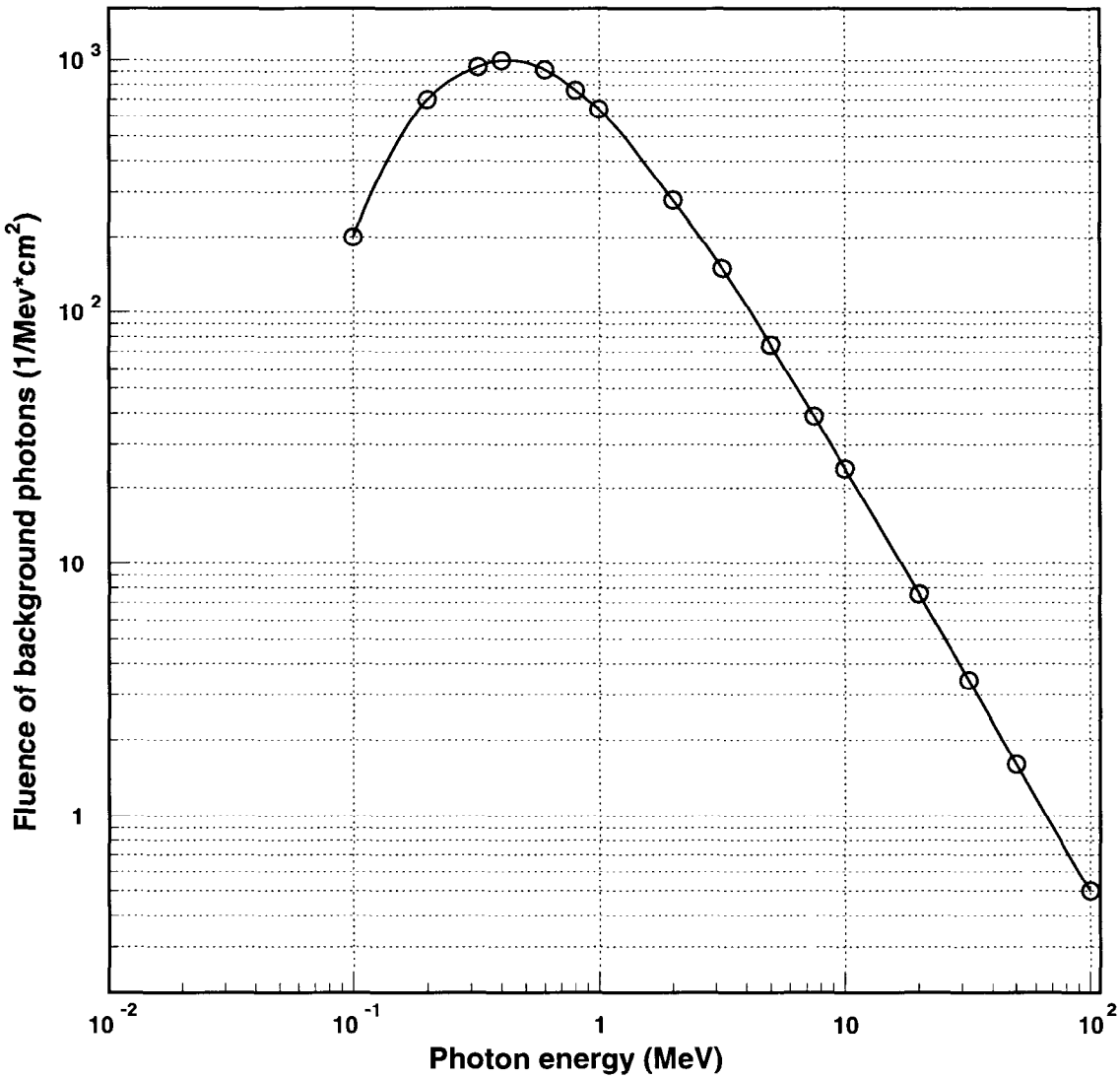

FIGURE 4. Simulated spectrum of photons in the vertex region. The cut–off energy was 25 keV. The vertex detector and the inner tracker were assumed to be massless during the simulation. Inclusion of realistic vertex and tracker detectors may shift the peak toward lower values.

will bring the occupancy of the first layer (cylinder) down to 0.8% for the same cell geometry. A threefold increase in radiation length X_0 of neon is an additional advantage over liquid argon. Multiple scattering in the system based on neon rather than argon is a factor of $\sqrt{3}$ smaller. A better momentum resolution can be

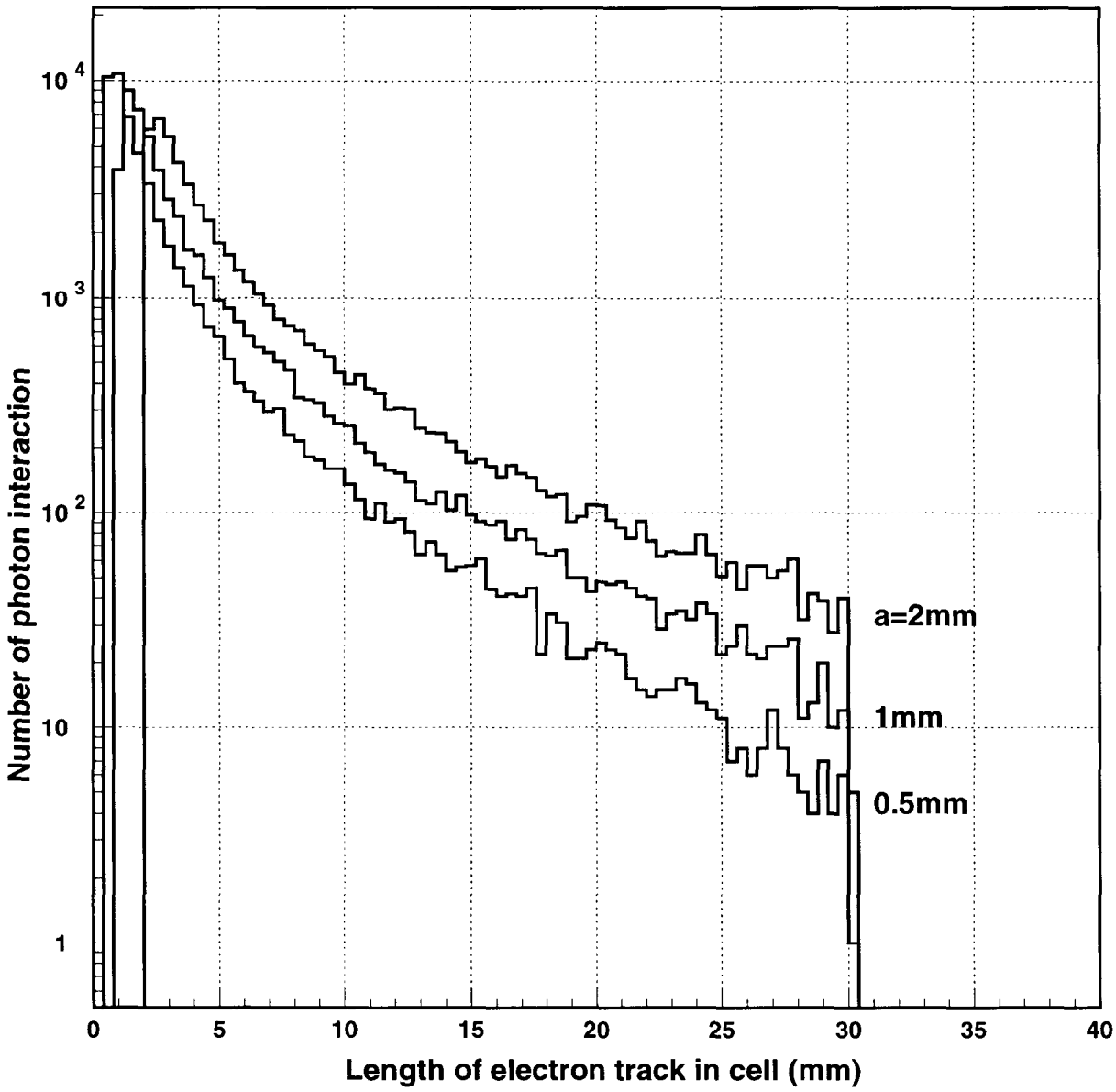

FIGURE 5. Distribution of lengths of electron trajectories resulting from the interaction of background photons in liquid argon of a single cell. Three different areas of the entrance surface of the cell were considered. The one dimension was fixed at 2mm while the second was 0.2, 1 or 2mm.

achieved for a given detector with liquid neon as a detection medium. Alternatively, we can build the detector with a smaller volume of the inner tracker or lower the magnetic field to obtain the same momentum resolution.

There is, however, a principal problem with the transport of electrons in pure liquid neon. The atomic polarizability is so small that the electron is trapped in a bubble in the liquid. Electrons thus have a very small mobility. It is known [4]

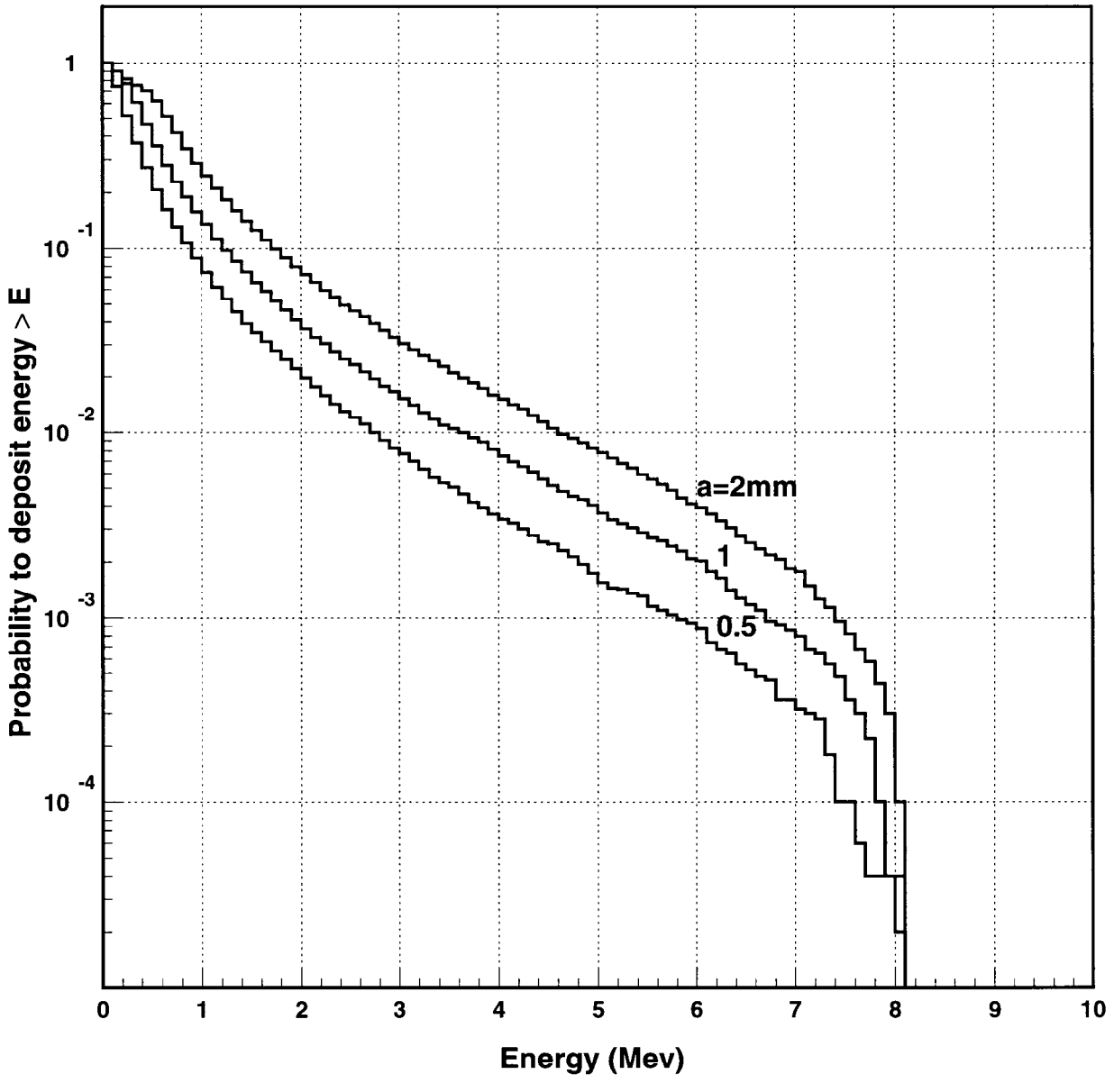

FIGURE 6. Integral spectrum, normalized to one, of the energy deposited in an individual cell. The simulations were done for three different cell geometries.

that this bubble is only marginally stable and we can suppose it is not present when a small amount of liquid argon or liquid methane is mixed with neon. More investigation is needed to find the best liquid.

Position Resolution

The cell dimensions of typically 1mm are too large to use the cell location as the only information about the position of the crossing fast particle. The vertex detector requires a precision of about $10\mu m$ and the interpolation of factors of about 100 is required in both measured directions. To obtain this high degree of interpolation the electric signal due to the motion of electron is treated in the optimal way. The optimal processing of the signals is presented in the Appendix. Principal ideas only are outlined here.

The sketch on the left hand side in Figure 7 represents the top view of the cell, that is, with a particle of interest coming perpendicular to the plane of paper. The cell dimension not visible in this projection is the depth traversed by the particle. The trapezoidal shape of the cell has been neglected and surfaces are assumed to be perfectly parallel. In the y direction the size of the cell is defined by a high voltage plane on one side ($y = 0$) and the electrons collecting electrodes at $y = d$ connected to preamplifiers. In the x direction the size of the cell is defined by the pitch of the electrode called a. The ionization produced by a fast particle originating in the intersection point is projected into a point (x_0, y_0). It is reminded here that liquid argon is a single carrier medium. Electrons move inside under the influence

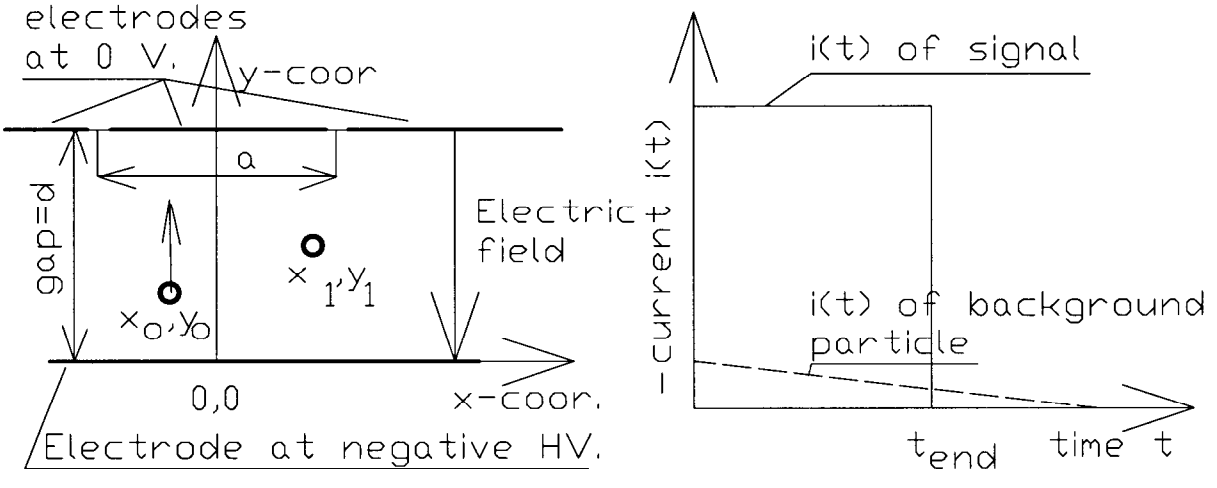

FIGURE 7. (LHS) The geometry and the electric field of several consecutive cell. The projection is such that the trajectories of particles of interest are seen as individual points. The movement of electrons produced at $(x_0; y_0)$ toward the electrode is indicated by an arrow. (RHS) the negative current waveform induced by i) signal particle–full line and ii) by a background particle–dotted line.

of the the applied electric field, while the velocity of positive ions is about 4 orders of magnitude smaller and they will be considered fixed during the signal processing time.

The plot on the right on Figure 7 shows the negative induced current due to the point–like ionization at x_0, y_0 at time 0 under the assumption of one dimensional geometry, that is, $a \gg d$. Right after the ionization was created electrons move to the collecting electrode with a constant velocity in a uniform electric field. This movement of electron induces a constant current in the electrode connected to a preamplifier. The current stops when signal electrons arrive at the electrode. The duration of the current pulse is the distance traveled by signal electrons divided by the drift velocity of electrons. In the coordinate system of Figure 7 $(d - y_0) = t_{end} \cdot v_{drift}$. Simply put, the duration of the signal current measures the y–coordinate of the particle.

The plot on the right on Figure 7 shows a dotted line indicating the current waveform produced by a background charged particle which crossed the cell along the y axis. The ionization was produced almost uniformly along the y axis. Signal electrons start to reach the collecting electrode close to it already at time zero and continue to arrive with a constant rate during the drift time of electrons across the full gap. The resulting current waveform is triangular and the area under the dotted line which is related to the total ionization of the background track is much smaller than the area under the signal current waveform due to the geometry of the cell. It is intuitive to see that we can measure the end point of the signal current waveform in the presence of background particles.

The position of the second coordinate, called x in Figure 7, of the particle within the cell is determined by the signal division among the consecutive electrodes of width a. (See the Appendix)

Other Limitations

Less sensitive regions

When the fast charged particle passes too close to the collecting electrodes, $(d - y_0) \ll d$, the signal electrons move only a short distance and the induced charge is small. One can arrive to the same conclusion from an equivalent point of view. The remaining positive charge at the production point x_0, y_0 induces an opposite polarity signal at the close–by electrode as the collected charge of negative electrons. The net signal is therefore small. To avoid the loss of sensitivity in one part of the cell, Figure 8 shows a perspective view of an array of cells where the direction of the electric field reverses along the cell. The least sensitive region in the lower half of the cell corresponds to the most sensitive region in its upper part. There is always a backup region behind a less sensitive region of a cell. The obvious drawback is the doubling the number of read out channels.

At this point it is noted that in order to avoid the dead layer of high voltage and of collecting electrodes it may be beneficial to introduce a small deviation (twist) from a perfect projection geometry. The background rejection and the resolution would be effected only slightly, while the small dead regions would be completely eliminated.

$\vec{E} \times \vec{B}$ *Effect*

The proposed cell provides the most precise position measurement along the direction of the motion of electrons (y coordinate in Figure 7 or ϕ coordinate in Figure 3). The deflection of a charged particle in a magnetic field is also measured along this direction. The achievable momentum resolution is thus optimized, however, we have to deal with the case where the electric field is perpendicular to the magnetic field leading to the maximal $\vec{E} \times \vec{B}$ effect. In the uniform electric field of the cells the effect causes signal electrons to drift along lines witch are at an angle α from the direction of the applied electric field and at a slightly reduced velocity.

The angle α is called a Lorentz angle in gas detectors and Hall angle in semiconductor detectors. It will be referred to as a Hall angle since rare gas liquids are closer to semiconductors than gases. Moreover, it will be assumed that some of the physics of Hall angle from semiconductors can be applied to liquids. The vector of average velocity of an electron under the influence of the electric field $\vec{E}$ and the magnetic field $\vec{B}$ equals (Equation 4 in Reference [5]):

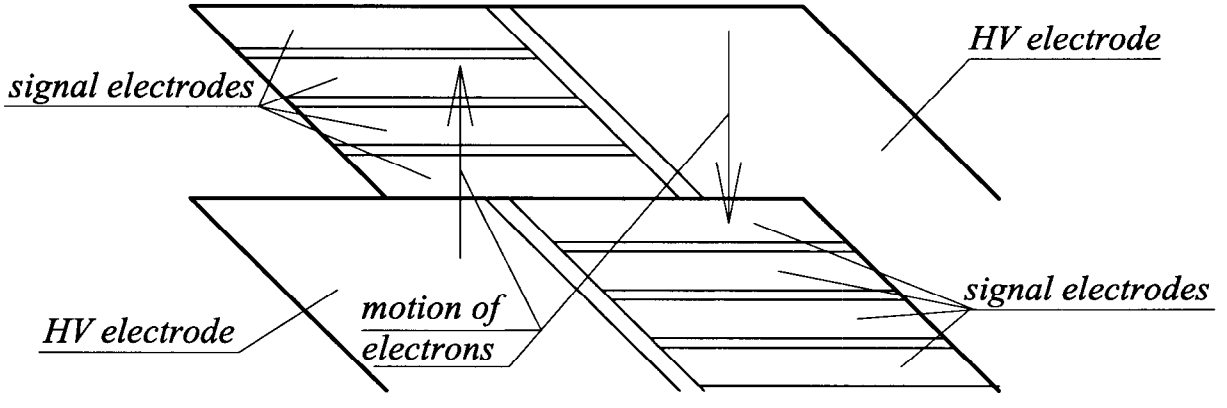

FIGURE 8. Perspective view of an array of cells where signal electrodes and HV electrode are swapping position along the trajectory of a fast particle. The direction of the electron motion is reversed in two parts of the cell.

$$\begin{pmatrix} dx/dt \\ dy/dt \\ dz/dt \end{pmatrix} = -\mu_r \begin{pmatrix} 1+\mu_H^2 B_x^2 & \mu_H^2 B_x B_y - \mu_H B_z & \mu_H^2 B_x B_z + \mu_H B_y \\ \mu_H^2 B_x B_y + \mu_H B_z & 1+\mu_H^2 B_y^2 & \mu_H^2 B_z B_y - \mu_H B_x \\ \mu_H^2 B_x B_z - \mu_H B_y & \mu_H^2 B_z B_y + \mu_H B_x & 1+\mu_H^2 B_z^2 \end{pmatrix} \begin{pmatrix} E_x \\ E_y \\ E_z \end{pmatrix} \tag{1}$$

where the reduced electron mobility μ_r, due to the presence of $\vec{B}$, is given by

$$\mu_r = \frac{\mu}{1+\mu_H^2 B^2} \tag{2}$$

where dx/dt,dy/dt and dz/dt are the components of the average velocity, μ is the electron mobility with all limitation due to the velocity saturation in liquids and μ_H is the Hall mobility.

The above system of 3 equations completely describes the electron transport within the liquid of the cells. Using the coordinate system of Figure 7 in which $E_x = E_z = 0$, $E_y = E$ and $B_y = B_z = 0$, $B_x = B$. This orientation of the magnetic field is exact for a cell located at 90^o from the intersecting beams. At other angles there is a non zero component of the magnetic field B_z (perpendicular to the plane of the paper). A substitution of these components of $\vec{E}$ and $\vec{B}$ into the tensor equation leads to:

$$\begin{pmatrix} dx/dt \\ dy/dt \\ dz/dt \end{pmatrix} = -\mu_r \begin{pmatrix} 0 \\ E \\ \mu_H B \cdot E \end{pmatrix} \tag{3}$$

The ratio $\frac{dz/dt}{dy/dt} = \mu_H B = \tan\alpha$ is the definition of the Hall angle α and the Hall mobility μ_H. The Hall mobility differs from the electron mobility by fine details of the average time between scattering events with and without applied magnetic field. The ratio of the Hall mobility to the electron mobility is a weak function of the magnetic field. We will assume that this ratio μ_H/μ is the same in liquids as in silicon where it is about 1.2 [5].

The effective value of the electron mobility in liquid argon is small. By dividing the electron velocity of $3mm/\mu s$ by the applied electric field of $5kV/cm$ the effective value of μ is $0.6 \times 10^{-2} m^2/Vs$. Assuming conservatively that the ratio μ_H/μ is between 1 and 2, the Hall mobility μ_H value is between $0.006 m^2/Vs$ and $0.012 m^2/Vs$. In a field of $3Tesla = 3Vs/m^2$ the tangent of the Hall angle is between 2% and 4%.

For a vertex cell at 90^o the trajectory of electrons deviates from the direction of the electric field only in the z coordinate which is not measured. In this location the only measurable effect of the magnetic field is the decrease of the electron drift velocity by a second order factor $1 + \mu_H^2 B^2 \approx 1.0001$, too small to consider. At other locations of the cell we will see a projection of the Hall angle directly into the measured coordinate x. The required precision of the interpolation is about 1% while $\tan\alpha$ can be as large as 4%. To bring the $\vec{E} \times \vec{B}$ correction down to a percent level it is sufficient to understand the value of the Hall mobility down to a 25% level.

Positive Space Charge

The mobility of positive ions in liquid argon is about four orders of magnitude smaller that the mobility of electrons. Positive ions drift very slowly to the HV electrode of the cell with a typical time of $3ms$ to be swept away. The presence of positive charges accumulated during this time influences the electric field within the cell and may modify the simple proportionality between the y position of the particle and the electron drift time. The induced signal due to the slow motion of accumulated positive charges can produce a noise like signal at the input of the preamplifiers.

Let us estimate the effect of the space charge in the first layer of the vertex detector at the distance $5cm$ from the interaction region. It was seen in the subsection describing the main background due to the conversion of photons that there are about 5.4 photon converting within one $0.5mm \times 2mm \times 30mm$ cell per bunch crossing. The average energy deposited by a photon in that cell, as can be seen form Figure 6, is slightly less than $0.5MeV$. Photon background deposits about $2.5MeV$ in a single cell per one bunch crossing. $25eV$ of energy is needed to produce 1 electron–ion pair, thus there are 10^5 pair produced in the volume of the cell per 1 crossing. The number of bunch crossing per second depends on the parameters of the machine and it is assumed here that there are $2 \cdot 10^4$ crossings per second. The rate of the ion production in the first cell is $2 \cdot 10^9 s^{-1}$ per volume of the cell $(= .5 \times 2 \times 30mm^3)$ or the volume intensity of the source s is $0.7 \cdot 10^8 mm^{-3} s^{-1}$.

It is also assumed that the ions are created uniformly in time and in the volume of the cell and from the moment of the creation move uniformly along the $-y$ axis of Figure 7 with velocity $v_{ion} = 300mm/s$ toward the HV electrode. Using the equation of continuity in one dimension with the source term s, one can find that the density of positive ions along the axis y has a triangular shape given by the expression $\rho(y) = (d-y) \cdot s/v_{ion}$. This form can be understood intuitively. Positive ions are swept away from the signal electrode region $y \leq d$ which is supplied only by the source term s. The HV electrode region $y \geq 0$ contains not only sourced ions but ions arriving from the whole length d. The mean density of positive ions in the cell is $2 \cdot 10^5 mm^{-3}$.

The presence of positive charges in the volume of the cell perturbs the uniform electric field of a charge free cell $E = U/d$. The size of the perturbation can be obtained by solving the Poisson equation

$$\frac{\partial U_p(y)}{\partial y^2} = -\frac{q \cdot \rho(y)}{\epsilon_0 \cdot \epsilon_r} \quad (= \frac{q \cdot s \cdot (y-d)}{\epsilon_0 \cdot \epsilon_r \cdot v_{ion}}), \tag{4}$$

where U_p is the potential of the perturbation, q is the absolute value of the electron charge, ϵ_0 permittivity of vacuum and ϵ_r is the relative dielectric constant of liquid argon. The boundary condition are $U_p(0) = U_p(d) = 0$ because the value of the potential on the electrodes is fixed. The Poisson equation with the ion density $\rho(y)$ can be solved directly by double integration. The solution, which satisfies the boundary condition is

$$U_p = \frac{q \cdot s}{\epsilon_0 \cdot \epsilon_r \cdot v_{ion}} \cdot (\frac{y^3}{6} - \frac{y^2 \cdot d}{2} + \frac{y \cdot d^2}{3}). \quad (5)$$

The electric field $E_p = -\partial U_p / \partial y$ is:

$$E_p = -\frac{q \cdot s}{\epsilon_0 \cdot \epsilon_r \cdot v_{ion}} \cdot (\frac{y^2}{2} - y \cdot d + \frac{d^2}{3}) \quad (6)$$

The electric field generated by the space charge of positive ions E_p is negative close to the HV electrode, that is, $y \geq 0$, then its value goes through zero and it is positive for $y \leq d$. The maximum absolute value of E_p at $y = 0$ is about $2V/mm$, which is 0.4% of the applied field of $500V/mm$. It seems that the perturbation of the electric field due to the positive ions does not represent a problem even within the cells positioned nearest to the interaction point.

The slow movement of positive ions is seen as a current by the preamplifier connected to the electrode of the cell. The average value of this current is just 1/2 of the rate of the ion production in the cell times the charge of individual ion or $\overline{I} = 1/2 \cdot 2 \cdot 10^9 \cdot qs^{-1} = 160pA$. This is a very small current when compare to the leakage currents of position sensing silicon detectors and can be easily accommodated by the preamplifier.

The spectral density of this current may be a more important issue. The current power spectral density of this current of $160pA$ viewed as being composed of individual uncorrelated electrons is of little importance for the signal processing time of interest, that is, about $1\mu s$. To see it, the "leakage current" of $160pA$ corresponds to the flow of 10^9 electron charges per second. In average an electrode collects 1000 charges within $1\mu s$. Poisson fluctuations of this number of charges is ± 30. This is negligible relative to a signal due to a particle produced at the interaction point and crossing the cell which is about 10^5 electrons.

The current due to the motion of positive ions is not composed from individual elementary charges. The average energy deposited in the cell by a background photon is $0.5Mev$ which produces $2 \cdot 10^4$ electrons. The uncorrelated charges are therefore much higher. However, due to the slower velocity of positive ions as compared to signal electrons (four orders of magnitude) the net effect is practically unchanged. We can conclude that the fluctuations in the current due to motion of positive charges does not degrade the performance of the vertex detector.

Now, all numbers needed to estimate the heating of liquid argon due to the drift of electrons and positive ions within a cell with $1kV$ applied are available. The sum of electron and ion currents is $320pA$ per one $0.5 \times 2mm^2$ entrance area cell of the innermost layer. Ohmic heating is $0.32\mu W$ per cell. With number of cells slightly less than 10^5 in this layer the total ohmic heating is only about $30mW$. this is much smaller than the expected heat dissipation of the front end electronics.

Inner Tracker

There is no reason to change the technology of the inner tracker from the proposed technology of the vertex detector. To keep the number of channels at reasonable level, the transverse dimensions of the cells can be increased. The background here is not a problem and individual cells can be made large enough so that the position resolution matches the mechanical tolerances of rather large layers of the tracker. The number of layers and the depth of individual layers is a compromise which leads to the best momentum resolution of the charged particles. If neon is used, we may even think of a tracker volume filled completely with the liquid neon.

This inner detector can be considered as a first class pre–shower detector. It may have just the right number of radiation length in front of the last position sensitive layer to convert a large enough percentage of high energy gammas. Clearly, it provides a very good position information for the shower localization.

The details of the momentum measurement for the charged particles will not be addressed here. The outer radius of the inner tracker has to be larger for the $100TeV$ collider than for $10TeV$ collider. Taking the outer radius of the tracker to be $1.2m$ at 90^o, the momentum resolution can be slightly better than $\delta P/P \lesssim 10^{-4}/GeV/c$. Thus $1TeV/c$ particles will be measured with 10% resolution and it will be possible to identify the charge of a particle with 3σ confidence level up to the momentum of $4TeV/c$.

Electromagnetic Calorimeter and Nose Calorimeter

In the previous studies [1] the choice of technology for the Electromagnetic Calorimeter was an accordion liquid argon calorimeter similar to one being under construction for the ATLAS Experiment at the CERN LHC. This is still a valuable option. To instrument two tungsten shield cones (noses) reaching close to the interaction point a different approach to the geometry of the calorimeter is needed. Once we have a valid technology for the nose calorimeters, we may as well apply it to the Electromagnetic calorimeter if it simplifies the system and provides an equivalent or superior performance.

The proposed technique is a refinement of the ATLAS liquid argon forward calorimeter [6] which was originally proposed for GEM for SSC [7]. The ATLAS and GEM unit cell of the calorimeter (see Figure 1 in Ref. [6]) consists of a solid brass rod of $4.5mm$ diameter inserted in a brass tube of inner diameter of $5mm$, resulting in a cylindrical gap of $250\mu m$ around the rod. The rod is fixed at the both ends and the gap spacing is maintained by an insulating quartz fiber wound around the rod, having the same diameter of $250\mu m$ as the gap filled with liquid argon.

An electric field is applied across the gap to collect the ionization electrons in the argon. The signal is then fed out, at the rear end of the rod through a low impedance cable to a preamplifier. The forward calorimeter is a matrix of such cells

with tubes mutually parallel in order to have the same sampling fraction through the depth of the calorimeter.

The design of the instrumented nose calls for a projective geometry, with finer sampling and smaller gap to maintain the shielding properties of the cone. The granularity should be very high to improve the discrimination against background. The density of the detector should be at least 95% of the density of the tungsten. To keep the constant energy sampling ratio independent of the radius in the projective geometry the gap has to change. We may change the radius of the tube or the radius of the rod.

More discrimination power relative to background can be gained by the longitudinal division of the cell along the shower direction. We can segment the outer surface of the rod and buried cables within the rod to connect all longitudinal segments out through the back.

The Electromagnetic Calorimeter can be constructed with similar cells. The material will not be the tungsten, but most likely brass or copper. Being further away form the intersection, the tube diameter may be larger. The main possible advantage of the projective geometry of these cells as compared to accordion (also in a projective geometry) is a superior pointing to the interaction region by rod cells. The design will require more complete simulations.

During the discussion with the theory group it was pointed out, that for some broad class of physics an ultimate energy and position resolution of the Electromagnetic calorimeter may be needed. An natural candidate would be a fully absorbing liquid xenon calorimeter. The cells of the calorimeter are practically identical to the cells of the vertex detector or tracker. The electronics will be much simpler, sensing only the total charge deposited in individual cells. Clearly, to work with liquid xenon requires a higher degree of a chemical cleanliness than when working with liquid argon.

The background situation and the trigger formation are well described on Page 64 of Reference [2].

Hadron Calorimeter

None of the energy generated by background photons is expected to penetrate into the hadronic calorimeter. The main background is due to the neutrons and Bethe–Heitler muons passing practically parallel to the beam direction. Calculations [2] shows that the background levels of neutrons and muons do not prevent a missing energy trigger down to 20 to 50 GeV level. Two options for the hadron calorimeter are considered. i) Liquid argon which has the advantage of being blind to neutrons and ii) Scintillator tile calorimeter which seems to be more economical. Both options are still valid. There was very little discussion about the hadron calorimeter options during the workshop.

Muon System

All 3 options mentioned in [1,2] are still under consideration. These are: i) Cathode strip chambers, ii) Threshold Cerenkov counter and iii) Long drift pad chambers with pad read out. The new strategy is to move the main precision muon detectors to a larger radius, to benefit of the rapid fall off of the background. A new muon absorber, in addition to calorimeters is introduced. In the forward directions, this strategy may include a Cerenkov detector measuring the angle of the muon. The strategy can be combined with a magnet supplying a solenoidal field for the inner tracker and the muon detector. To avoid wasted, expensive, magnetic field volume an additional bending takes place in the absorber. The momentum information from the muon system is combined with the measurement of the momentum from the inner tracker to improve the resolution and to reject muons originating from pion decays.

Appendix. Position resolution in a proposed cell

We will use the coordinate system shown on the left hand side of Figure 7. The ionization produced by a particle created in the interaction point is seen as a point ionization in this view. Let us concentrate on the particle which produced a unit of ionization charge at the point $(x_1, y_1) = (0.9, 1)$ in the coordinate system, where we have fixed the cell dimension at $a = d = 2mm$.

Electrons created by the ionizing particle move along a straight line $x = x_1 = 0.9$ toward the electrode while positive ions move so slowly that we will consider them being fixed at point x_1, y_1 during the signal processing time. While electrons are moving the signal current is induced on all electrodes "visible" from the electron trajectory. While the concept of the induced current is intuitive, here we will use more often a closely related concept of the induced charge on an electrode. The induced charge is simply the time integral of the induced current. Our preference to use the integral of the current rather than the current itself is due to the different shape of noise spectral density in both cases.

We have seen that the effective leakage current of a cell is very small. The parallel noise at the input of the preamplifier is negligible and the only relevant noise source is the series noise of the preamplifier which is proportional to the frequency. We can transform the series noise into a white noise, that is, the noise which has the uniform density independent of frequency, by integrating the input signal. This pre–whitening filter transforms induced current into induced charge. When processing signals from the first layer of the vertex detector (where the leakage current is not completely negligible due to the cumulative current from motion of positive ions) to obtain white noise, we have to integrate with an integration constant equal to the noise time corner τ. Here we will assume that $\tau \gg 1\mu s$, $1\mu s$ being the processing time for electron signals.

The signal induced at any electrode by the presence of charge Q located at position x, y within the gap can be obtained by solving the direct electrostatic problem, that is, by solving the Laplace equation of electrostatics with the charge Q at x, y and all electrodes (boundaries) at zero potential. A charge induced at any particular electrode is, according to Gauss's theorem, the surface integral of the electric field ending on the surface times dielectric constant ϵ_0. When the charge is moving within the gap, in order to know the induced charges at the electrode produced by the charge Q in the next position we have to find a complete solution for a different electrostatic field, possibly a time consuming approach.

We can apply Green's Reciprocation Theorem [8] to be able to know the field induced by a charge Q located at any arbitrary point x, y on a given electrode with only one solution of the electrostatic field problem. The final result of the application of the Green's Reciprocation Theorem can be stated: the charge induced at a given electrode by a charge Q located at x, y equals to the product of the charge Q times the value of the potential of an induction (auxiliary) field U at the point x, y. The induction (auxiliary) field is the solution of an electrostatic problem, when the value of 1 is applied at the electrode on which we want to know the induced charge and 0 on all other electrodes of the problem and the space between is free of any charges.

The induction (auxiliary) field for the central electrode of Figure 7, ($y = d$, $-a/2 < x < a/2$) can be found in a closed form the by method of conformal mapping. In the volume of the cell, that is, for $0 < y < d$ one can write:

$$U(x,y) = \frac{1}{\pi}\left\{\arctan\left[\tanh(\pi\frac{x+a/2}{2d})\cdot\tan(\pi\frac{y}{2d})\right] - \arctan\left[\tanh(\pi\frac{x-a/2}{2d})\cdot\tan(\pi\frac{y}{2d})\right]\right\}, \tag{7}$$

or:

$$U(x,y) = \frac{1}{\pi}\left\{\arctan\left[\tanh(\beta)\cdot\tan(\gamma)\right] - \arctan\left[\tanh(\alpha)\cdot\tan(\gamma)\right]\right\}, \tag{8}$$

where α (no relation to the Hall angle), β and γ have the following dependence on the x, y coordinates:

$$\alpha = \pi\frac{x-a/2}{2d};\ \beta = \pi\frac{x+a/2}{2d};\ \gamma = \pi\frac{y}{2d} \tag{9}$$

The charge induced on the central electrode by the moving electrons is $Q_-(t) = -Q\cdot U(x_1, y = y_1 + v\cdot t)$ during their drift time $\tau = (d - y_1)/v$ where v is the drift velocity of electrons in the liquid. The negative sign corresponds to a standard convention of electron having a negative charge. When electrons arrive onto the collected electrode, U on the electrode equals 1, and they induce the full charge on the electrode. This full induction is equivalent to an actual collection of the electrons by the electrode. The charge induced by positive ions is $Q_+ = Q\cdot U(x_1, y_1)$

and does not change with time. The net induced charge is the sum of the charges induced by electrons and positive ions: $Q(t) = Q_-(t) + Q_+$. This time dependence can be seen from the left hand side of Figure 9. At time zero the electrons and positive ions are at the same location and the net induced charge is zero. After collecting all electrons the net negative charge on the electrode is less than 1 due to the induction of opposite polarity charges of ions remaining within the cell's volume.

The charge induced on the neighboring electrodes can be found from the translational symmetry of the geometry along the x-axis. The charge induced on an electrode centered at $x_c = 0 + k \times a$, (k being an integer), by a charge located at x, y is the same as the charge induced on the central electrode by the charge located at point $(x - k \times a, y)$, which is given by Eg. 7 as $U(x - k \times a, y)$. The right hand side of Figure 9 shows the induced charge on the two electrodes adjacent to the central electrode. The continuous line corresponds to the charge induced on the electrode with its center at $x = a$, that is, right from the central electrode. The particle crossed the cell at $x_1 = 0.9$, not too far from the boundary between these two cells at $x = 1$. During the first part of the electron drift time, the charge

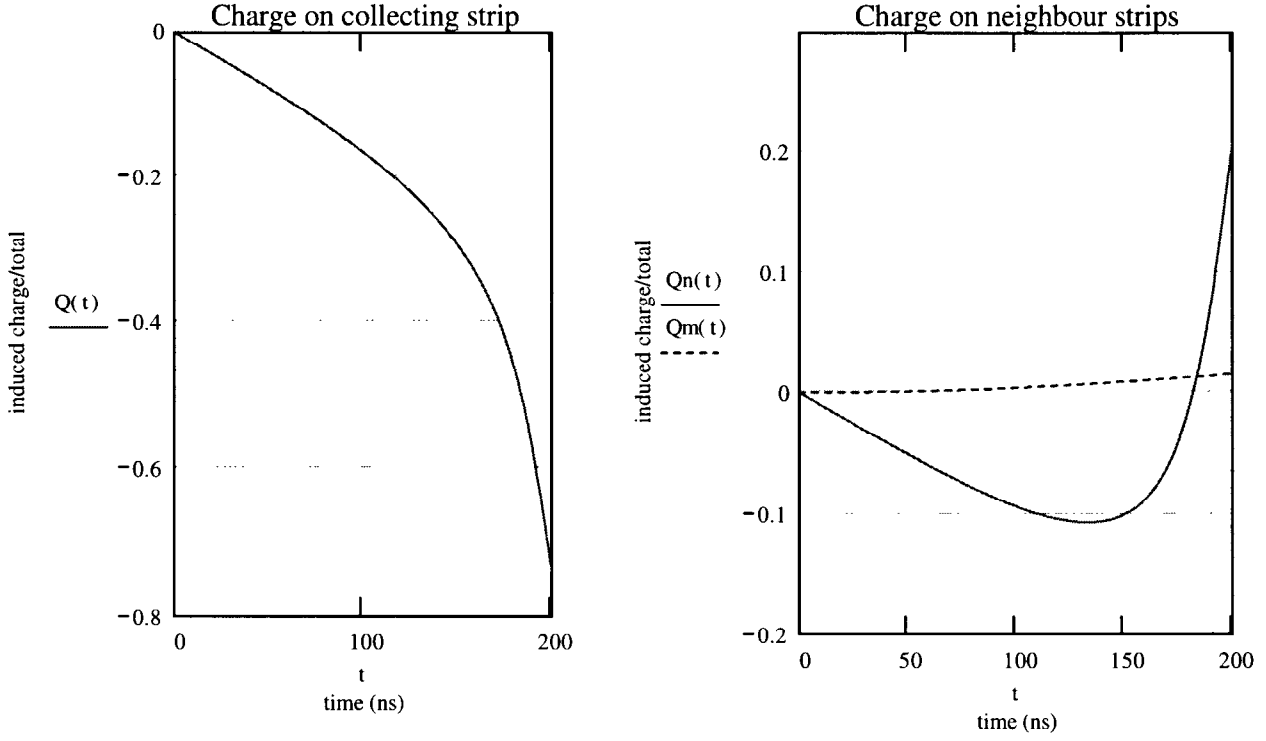

FIGURE 9. Time dependence of induced charge normalized to 1 by ionization at point $(x_1, y_1) = (0.9, 1)$ seen: i) on signal collected electrode (left hand side) and ii) on the neighbor electrodes (right hand side). The drift velocity of electrons was $5\mu m/ns$. After 200 ns of electron collection time, all waveforms remain constant.

induced on this neighbor cell is only slightly smaller than the charge induced on the central electrode. However, during the final moments of the electron drift, electrons are headed to the central electrode and the amount of negative charge induced by electrons decreases. When electrons arrive to the central electrode the only charge induced on the neighbor electrode is the positive charge due to remaining ions.

The shapes of the induced charge signals on each electrode depend only on 3 parameters and on the noise in the read outs. The 3 parameters are: x and y coordinates of the crossing particle and the amount of charge Q produced by the particle. It is assumed that the time of the particle crossing is known from the timing of the bunch crossing. The problem is to find these 3 parameters from the measurable waveforms of the induced charge on the electrodes of interest. Noise present in all read out channels is a stochastic process and we will use statistical methods to infer the best estimates of these 3 parameters from observed waveforms for each event.

The noise superposed on the ideal waveforms is white as proven above. In the time domain (that is, when we are inspecting a measured noisy waveform as function of time as presented on an oscilloscope) the white noise means that the fluctuations at different times are all the same and that there is no correlation between fluctuations at any two different times. We can think to sample induced charges (and noise) from all electrodes and to find x, y and Q to "fit" shapes of all recorded waveforms. We will use the most powerful statistical tool, the maximum likelihood method for our analysis. The analysis presented here is similar to that of [9].

The logarithm of the likelihood function L is

$$\ln(L) = \sum_k \sum_n \left\{ \ln\left[\frac{1}{\sqrt{2\pi}\cdot\sigma_k(t_n)}\right] - \frac{[Q_k(x,y,Q,t_n) - m_k(t_n)]^2}{2\sigma_k^2(t_n)} \right\}, \qquad (10)$$

where $\sum_k$ denotes the summation through the waveform produced by different electrodes k, $\sum_n$ is the summation through different sampling times t_n, $m_k(t_n)$ is the measured (sampled) waveform from the k^{th} electrode at the sampling time t_n and $Q_k(x,y,Q,t_n)$ is the value of the noiseless waveform from k^{th} electrode at time t_n when a particle crossed the cell at the point x, y and produced the total ionization charge Q, and $\sigma_k(t_n)$ is the square root of the variance of the k^{th} waveform at time t_n.

The sampled waveform has to be passed through a bandwidth limited or Nyquist filter before being sampled. This filter limits also the white noise of individual samples. For our case $2\sigma_k^2(t_n) = C_{tot}^2 \cdot e_s^2/\Delta t$ where C_{tot} is the total input capacitance of individual electrodes including the capacitance of the input transistor and the capacitance of connections, e_s^2 is the voltage power spectral density of the preamplifier and Δt is the sampling interval.

The noiseless waveform from the k^{th} electrode can be written as:

$$Q_k(x,y,Q,t_n) = Q\cdot[U(x-ka,y) - U(x-ka,y+v\cdot t_n)] \quad 0 < t_n < \tau \qquad (11a)$$

$$Q_k(x,y,Q,t_n) = Q\cdot[U(x-ka,y) - \delta_k] \quad \tau < t_n < T, \qquad (11b)$$

where τ is the drift time of electrons from the creation point x, y to the electrode at $x = d$.

$$\tau = (d - x)/v \tag{12}$$

and we have introduced a total processing time T. This time must be shorter than the time between two consecutive bunch crossings. Practically there is very little improvement beyond $T = 3\tau_{max} = 3d/v$. Eq. 10 can be now be rewritten as

$$\ln(L) = N - \sum_k \sum_n \frac{[Q_k(x, y, Q, t_n) - m_k(t_n)]^2}{C_{tot}^2 e_s^2/\Delta t}, \tag{13}$$

where $Q_k(x, y, Q, t_n)$ is given by Eqs. 11 and N is a normalization factor. Following the method of [9] we will linearize $Q_k(x, y, Q, t_n)$ as functions of the unknown parameters x, y and Q at a starting point $x^{(0)}, y^{(0)}$ and $Q^{(0)}$ of an iteration process.

$$\begin{aligned} Q_k(x, y, Q, t_n) = Q_k(x^{(0)}, y^{(0)}, Q^{(0)}, t_n) + \frac{\partial Q_k(x, y, Q, t_n)}{\partial x} \cdot (x - x^{(0)}) \\ + \frac{\partial Q_k(x, y, Q, t_n)}{\partial y} \cdot (y - y^{(0)}) + \frac{\partial Q_k(x, y, Q, t_n)}{\partial Q} \cdot (Q - Q^{(0)}) \end{aligned} \tag{14}$$

All partial derivatives in Eq. 14 are meant to be taken at $x^{(0)}, y^{(0)}$ and $Q^{(0)}$ and do not depend on x, y and Q. We substitute Q from Eq. 14 into Eq. 13 and obtain a linearized expression for the logarithm of likelihood to be maximized relative to 3 parameters x, y and Q.

$$\begin{aligned} \ln(L) = N - \sum_k \sum_n \frac{\Delta t}{C_{tot}^2 e_s^2} \cdot \Bigg[Q_k(x^{(0)}, y^{(0)}, Q^{(0)}, t_n) + \frac{\partial Q_k(x, y, Q, t_n)}{\partial x} \cdot (x - x^{(0)}) \\ + \frac{\partial Q_k(x, y, Q, t_n)}{\partial y} \cdot (y - y^{(0)}) + \frac{\partial Q_k(x, y, Q, t_n)}{\partial Q} \cdot (Q - Q^{(0)}) - m_k(t_n) \Bigg]^2 \end{aligned} \tag{15}$$

Partial derivatives of $\ln(L)$ with respect to x, y and Q must equal to zero leading to a system of 3 linear equations:

$$\begin{aligned} (x - x^{(0)}) \sum_{k,n} [\frac{\partial Q_k(t_n)}{\partial x}]^2 + (y - y^{(0)}) \sum_{k,n} [\frac{\partial Q_k(t_n)}{\partial x}] \cdot [\frac{\partial Q_k(t_n)}{\partial y}] + \\ (Q - Q^{(0)}) \sum_{k,n} [\frac{\partial Q_k(t_n)}{\partial x}] \cdot [\frac{\partial Q_k(t_n)}{\partial Q}] = - \sum_{k,n} [Q_k(t_n) - m_k(t_n)] \frac{\partial Q_k(t_n)}{\partial x} \end{aligned} \tag{16a}$$

$$\begin{aligned} (x - x^{(0)}) \sum_{k,n} [\frac{\partial Q_k(t_n)}{\partial x}] \cdot [\frac{\partial Q_k(t_n)}{\partial y}] + (y - y^{(0)}) \sum_{k,n} [\frac{\partial Q_k(t_n)}{\partial y}]^2 + \\ (Q - Q^{(0)}) \sum_{k,n} [\frac{\partial Q_k(t_n)}{\partial y}] \cdot [\frac{\partial Q_k(t_n)}{\partial Q}] = - \sum_{k,n} [Q_k(t_n) - m_k(t_n)] \frac{\partial Q_k(t_n)}{\partial y} \end{aligned} \tag{16b}$$

$$(x-x^{(0)})\sum_{k,n}[\frac{\partial Q_k(t_n)}{\partial x}]\cdot[\frac{\partial Q_k(t_n)}{\partial Q}]+(y-y^{(0)})\sum_{k,n}[\frac{\partial Q_k(t_n)}{\partial y}]\cdot[\frac{\partial Q_k(t_n)}{\partial Q}]+$$
$$(Q-Q^{(0)})\sum_{k,n}[\frac{\partial Q_k(t_n)}{\partial Q}]^2=-\sum_{k,n}[Q_k(t_n)-m_k(t_n)]\frac{\partial Q_k(t_n)}{\partial Q} \qquad (16c)$$

All partial derivatives in Eqs. 15 and 16 have an explicit analytical form. Here, just for completeness, are the derivatives of $U(x,y)$

$$\frac{\partial U(x,y)}{\partial x}=\frac{\sin\gamma\cos\gamma}{2d}\left(\frac{1}{\cos^2\gamma+\sinh^2\beta}-\frac{1}{\cos^2\gamma+\sinh^2\alpha}\right) \qquad (17a)$$

$$\frac{\partial U(x,y)}{\partial y}=\frac{1}{2d}\left(\frac{\sinh\beta\cdot\cosh\beta}{\sinh^2\beta+\cos^2\gamma}-\frac{\sinh\alpha\cdot\cosh\alpha}{\sinh^2\alpha+\cos^2\gamma}\right), \qquad (17b)$$

where α,β and γ were defined in Eq. 9.

The first solution of linear system of equations 16 gives values for x,y and Q. These value become $x^{(0)},y^{(0)}$ and $Q^{(0)}$, that is, initial values for the next iteration. All derivatives have to be recalculated at $x^{(0)},y^{(0)}$ and $Q^{(0)}$ and the system of Eqs. 16 have to be solved again. This iteration process has to be repeated until the respective differences between $x^{(0)},y^{(0)}$ and $Q^{(0)}$ and x,y and Q are sufficiently small. We will not attempt to prove that the process converges in general to the physical solution.

Let us study the statistical properties of the solution thus obtained. The likelihood function in Eq. 15 can be formally regarded as a probability density function for the parameters x,y and Q viewed as random variables while the final values $x^{(0)},y^{(0)}$ and $Q^{(0)}$ are the expected values. The logarithm of the probability density function $p(x,y,Q)$ for jointly normal random variables x,y and Q is written in its canonical form as:

$$p(x,y,Q)=N_{cf}-\frac{1}{2}\overline{X}^T\cdot\mathcal{M}^{-1}\cdot\overline{X}, \qquad (18)$$

where N_{cf} is the normalization constant, $\overline{X}$ is the column vector composed of $(x-x^{(0)})$; $(y-y^{(0)})$; $(Q-Q^{(0)})$, $\overline{X}^T$ is its transposed (row) vector and $\mathcal{M}^{-1}$ is the inverse of the symmetric, positive–definite variance matrix [10]. $\overline{X}^T\cdot\mathcal{M}^{-1}\cdot\overline{X}$ is the quadratic form of this three-variate normal distribution. We have to carry on the square of the polynomial terms in brackets of Eq. 15 and try to express it in the form of Eq. 18. After some manipulations the inverse of the variance matrix $\mathcal{M}^{-1}$ can be written

$$\frac{2\Delta t}{C_{tot}^2e_s^2}\sum_{k,n}\begin{pmatrix}[\frac{\partial Q_k(t_n)}{\partial x}]^2 & [\frac{\partial Q_k(t_n)}{\partial x}]\cdot[\frac{\partial Q_k(t_n)}{\partial y}] & [\frac{\partial Q_k(t_n)}{\partial x}]\cdot[\frac{\partial Q_k(t_n)}{\partial Q}]\\ [\frac{\partial Q_k(t_n)}{\partial x}]\cdot[\frac{\partial Q_k(t_n)}{\partial y}] & [\frac{\partial Q_k(t_n)}{\partial y}]^2 & [\frac{\partial Q_k(t_n)}{\partial y}]\cdot[\frac{\partial Q_k(t_n)}{\partial Q}]\\ [\frac{\partial Q_k(t_n)}{\partial x}]\cdot[\frac{\partial Q_k(t_n)}{\partial Q}] & [\frac{\partial Q_k(t_n)}{\partial y}]\cdot[\frac{\partial Q_k(t_n)}{\partial Q}] & [\frac{\partial Q_k(t_n)}{\partial Q}]^2\end{pmatrix}, \qquad (19)$$

because the absolute term $\sum_{k,n}\left[Q_k(x^{(0)},y^{(0)},Q^{(0)},t_n)-m_k(t_n)\right]^2$, which gives the information about the statistical quality of the solution, is absorbed in the normalization term N_{cf} and the coefficients of all linear terms sum up to zero. This can be understood heuristically from the condition of maximum of likelihood function L at the solution point. More directly, it can be noticed that the factors multiplying the vector $(x-x^{(0)})$, $(y-y^{(0)})$ and $(Q-Q^{(0)})$ form (apart from a multiplication constant) the right hand side vector of the system of Eqs. 16. At the end of the iteration sequence $x=x^{(0)}$, $y=y^{(0)}$ and $Q=Q^{(0)}$, that is, the final system had a trivial solution. The matrix of the system is not singular and the only way to obtain the zero vector as a solution is by having the right hand side of the system of Eqs. 16 equal to zero.

If the sampling interval Δt is sufficiently small we can replace $\Delta t\sum_n$ with $\int_0^T dt$. The inverse of the variance matrix $\mathcal{M}^{-1}$ then becomes

$$\frac{2}{C_{tot}^2 e_s^2}\sum_k\begin{pmatrix}\int_0^T[\frac{\partial Q_k(t)}{\partial x}]^2dt & \int_0^T[\frac{\partial Q_k(t)}{\partial x}][\frac{\partial Q_k(t)}{\partial y}]dt & \int_0^T[\frac{\partial Q_k(t)}{\partial x}][\frac{\partial Q_k(t)}{\partial Q}]dt\\ \int_0^T[\frac{\partial Q_k(t)}{\partial x}][\frac{\partial Q_k(t)}{\partial y}]dt & \int_0^T[\frac{\partial Q_k(t)}{\partial y}]^2dt & \int_0^T[\frac{\partial Q_k(t)}{\partial y}][\frac{\partial Q_k(t)}{\partial Q}]dt\\ \int_0^T[\frac{\partial Q_k(t)}{\partial x}][\frac{\partial Q_k(t)}{\partial Q}]dt & \int_0^T[\frac{\partial Q_k(t)}{\partial y}][\frac{\partial Q_k(t)}{\partial Q}]dt & \int_0^T[\frac{\partial Q_k(t)}{\partial Q}]^2dt\end{pmatrix} \quad (20)$$

Integrals in Matrix 20 can be numerically calculated and the matrix inverted. We present here only the most important parameters. The square root of the diagonal terms of the inverted matrix are the resolutions in x, y and Q respectively. Figures 10 and 11 show the position resolutions in both coordinates as a function of the position within the cell for two different cell geometries. The values of the resolutions in both directions are shown only for $y<1.8mm$, that is for 90% of the cell's area. The resolution degrades for an incidence $y\leq d=2mm$ as explained in the main section. To obtain the position information signals from the total of 3 consecutive cells, $k=-1,0,1$ were considered for $a=2mm$ geometry (Figure 10) and the total of 5 cells, $k=-2,-1,0,1,2$, were considered for $a=1mm$ cell of Figure 11. All other parameters were the same for both simulations ($d=2mm$, $e_s=4nV/\sqrt{Hz}$, $C_{tot}=5pF$, $T=1.5\mu s$, $v=3mm/\mu s$). The charge produced by the passing particle was assumed to be $12fC$, that is, the average charge produced by a minimum ionizing particle traversing $2cm$ of liquid argon. Values of all plotted σ are proportional to e_s and C_{tot} and inversly proportional to the signal charge Q as can be seen directly from the form of the inverse variance matrix $\mathcal{M}^{-1}$ in Equation 20 and Equation 11. Scaling with the other parameters is more complex.

The value of $e_s=4nV/\sqrt{Hz}$ is modest. The first transistor of the preamplifier has to have a transconductance of only $0.7mS$. This value of transconductance can be reached with the drain current of $2.5\times 20\mu A=50\mu A$, $20\mu A$ being the "Maxwell's"current requirement, implying a modest power consumption of the front end electronics in the region of $0.2mW$/channel. The total power consumption of the vertex can be in 20 to 50W region.

The resolution shown is better than the mechanical stability of the physical layers of liquid argon within the inner tracker. If the background is not a problem we

can save on the number of channels by increasing the cell size until the electronic resolution matches the mechanical tolerances.

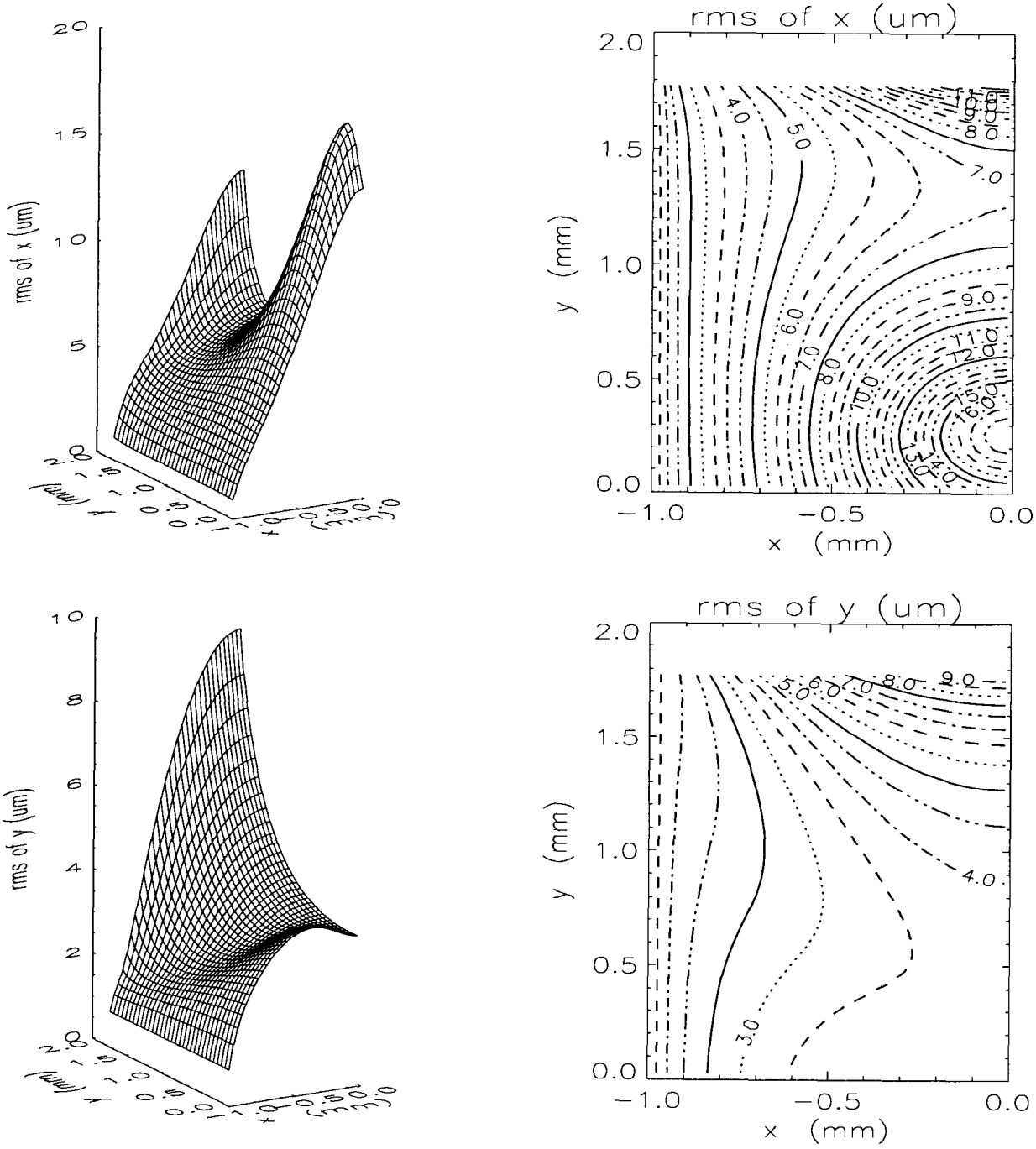

FIGURE 10. Position resolution along coordinate i) x obtained mainly by signal sharing (upper part) and ii) y obtained mainly from the drift time. Only 1/2 of the cell's size of $2mm$ in the x–direction is shown. The resolution is symmetrical around the y–axis ($x = 0$)

The optimal algorithm to obtain the position of a crossing charged particle may seem to be too involved to be practical. There are two answers to this objection.

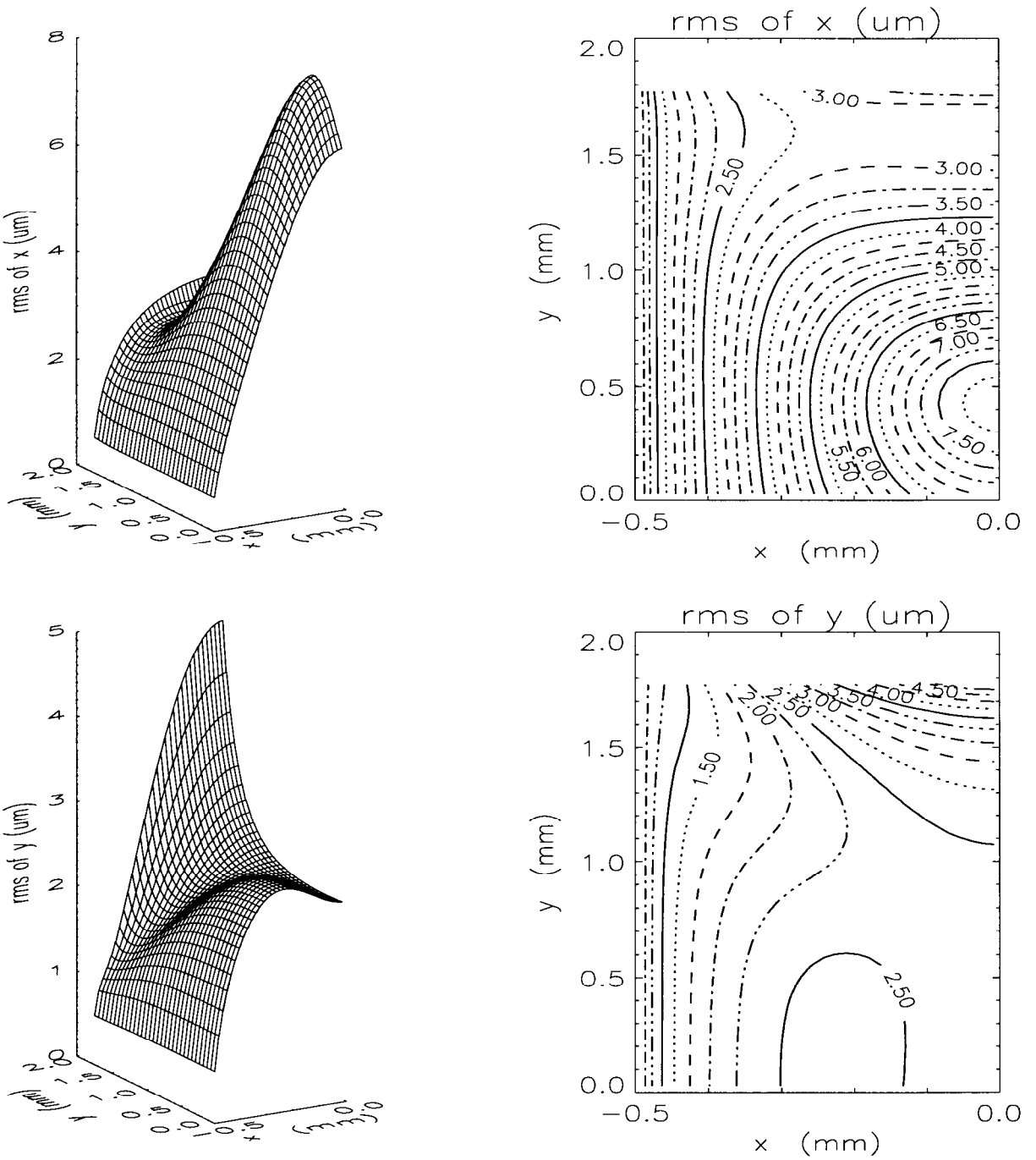

FIGURE 11. Position resolution along coordinate i) x obtained mainly by signal sharing (upper part) and ii) y obtained mainly from the drift time. Only 1/2 of the cell's size of $1mm$ in the x–direction is shown. The resolution is symmetrical around the y–axis ($x = 0$)

1. Given the increase of the power of processors with time, it may be practical, at the time of the detector construction, to put enough computing power right next to liquid argon layers to follow the optimum approach.

2. For a limiting case of $a \gg d$, that is, for one dimensional geometry a complete analytical calculation of maximum likelihood method can be carry through with two unknowns y and Q. The obtainable resolution in y is

$$\sigma_y = \frac{e_s \cdot C_{tot} \cdot d}{Q} \cdot \sqrt{\frac{3v}{2(d-y)}}. \tag{21}$$

   A simple analysis of the precision attainable with a linear centroid finding filter gives the resolution of only $2/\sqrt{3} = 1.15$ times wider. A degradation of the position resolution by 15% is acceptable. Very likely, it is possible to develop a simple linear filter for the complete problem to determine both coordinates which is practical to implement and which does not degrade the resolution more than 15 to 30%.

Conclusions

In this contribution we have described a possible detector around an intersection region of a high energy $\mu^+\mu^-$ collider. We have considered the challenges coming from an intense background arriving at the same time as the very rare interactions of interest. The new technology for the vertex detector and inner tracker is based on long projective cells filled with liquid argon and pointing toward the interaction point. Such a detector is radiation hard and less sensitive to background. The performance of such a detector was analyzed in details. The results indicate that this technology would perform according the physics specification.

Moreover, this contribution proposes to instrument the two conical shape tungsten shields to improve the physics potential of the detection system and specifies a particular technology of achieving it.

A new option for the technology of the electromagnetic calorimeter was proposed. An improved muon system was shortly discussed.

REFERENCES

1. The $\mu^+\mu^-$ Collider collaboration, *$\mu^+\mu^-$ Collider–A Feasibility Study*, Snowmass DPF July 1996 Workshop, **BNL–52503, Fermi Lab–Conf.–96/092, LBNL–38946**, (1996); http://www.cap.bnl.gov/mumu/book.html
2. Ch. M. Ankenbrandt et al., (Muon Collider Collaboration) *Phys. Rev. Special Topics* **2**, 081001, (1999). This excellent review contains up to date list of references.
3. S. Geer and J. Chapman, in *Proceedings of 1996 DPF/DPB Summer Study on High–Energy Physics*; Fermilab Report No. **FERMILAB–CONF–96–375.**

4. Werner F. Schmidt, *Liquid state electronics of insulating liquids*, Boca Raton: CRC Press, 1997.
5. A. Castoldi at al., *Nucl. Instrum. and Meth.* **A399**, 227-243(1997).
6. M. I. Ferguson et al., *Nucl. Instrum. and Meth.* **A383**, 399-408 (1996).
7. GEM, Technical Design Report, April 30, 1993, GEM–TN–93–262, SSCL–SR–1219, Page 5–52.
8. John D. Jackson, *Classical Electrodynamics*, Second Edition, John Wiley & Sons, New York, (1975), Problem 1.12, Page 51.
9. G. Bertuccio et al., *Nucl. Instrum. and Meth.* **A322**, 271-279 (1992).
10. B. R. Martin, *Statistics for Physicist*, Academic Press, London and New York, (1971), Page 30.